RESEARCH ARTICLE

Check for updates

Self-assembled manganese acetate@tin dioxide colloidal quantum dots as an electron-transport layer for efficient and stable perovskite solar cells†

Yutao Li,[a] Chenyu Zhao,[a] Lexin Wang,[a] Lin Fan, [ID] [a,b] Maobin Wei,[a,b] Huilian Liu,[a,b] Xiaoyan Liu,[a,b] Jinghai Yang, [ID] *[a,b] Fengyou Wang [ID] *[a,b] and Lili Yang [ID] *[a,b]

An SnO_2 electron-transport layer (ETL) is a critical and mainstream component utilized in perovskite solar cells (PSCs) on account of its exceptional photoelectric performances and low-temperature fabrication process. Nevertheless, a significant number of defects on the surface of SnO_2 quantum dots (QDs) can lead to QD agglomeration in dispersion and poor film quality, ultimately compromising the power conversion efficiency (PCE) and stability of devices. In this study, we developed multifunctional manganese acetate $(Mn(Ac)_2)$-stabilized SnO_2 quantum dots (Mac-SnO_2 QDs) and utilized them to prepare ETLs for PSCs. The C=O groups of $Mn(Ac)_2$ can terminate the Sn^{4+} dangling bonds on Mac-SnO_2 QDs, thereby preventing QD agglomeration, facilitating the preparation of a uniform film with good electrical properties. In addition, Mn^{2+} can permeate upward into the perovskite film, passivating I^- at the grain boundary and reducing perovskite bulk defects. Moreover, the perovskite grown on Mac-SnO_2 releases residual stress, which can improve device performance and stability. As a consequence, Mac-SnO_2 PSCs achieved a high PCE of 23.36% with improved stability. This successful approach of utilizing an organic acid salt to modify SnO_2 QDs provides a facile and efficient strategy for enhancing the efficiency and stability of PSCs.

1. Introduction

Interest in organic–inorganic hybrid perovskite solar cells (PSCs) has recently surged in the photovoltaic field owing to their remarkable optoelectronic performances, such as high carrier mobility, low exciton binding energy, long carrier diffusion length, and excellent absorption coefficient.[1–3] Since the advent of the first PSCs, their certified power conversion efficiency (PCE) has boomed to 26.1% over the past dozen years, which is comparable to mature commercial silicon cells.[4–6] One of the critical factors for achieving advanced devices is the application of inorganic metal oxides, such as ZnO, SnO_2, and TiO_2, as electron-transport layers (ETLs).[7–10] These ETLs play a key role in extracting and separating carriers, have high transmittance to allow light into the absorbed layer, and display well-matched energy levels with the perovskite material. Currently, SnO_2 stands out among the many ETLs because of its excellent photoelectric properties, high

optical transmittance, exceptional ultraviolet (UV) stability, and suitability for low-temperature preparation.[11–15] However, similar to other inorganic metal oxides, the surface of SnO_2 quantum dots (QDs) possesses a significant number of metallic dangling bonds, leading to disordered surface charges. Consequently, QDs will attract each other because of van der Waals interaction, resulting in instability and agglomeration of the QDs.[16,17] Upon film formation, the material suffers from pinholes and non-uniformity, leading to poor film quality. Moreover, the presence of Sn dangling bonds on the surface can capture hydroxyl groups during film formation and induce perovskite degradation.[18–20] These surface defects inevitably trap electrons, resulting in carrier non-radiative recombination, thus affecting interface electron transport.

To mitigate film surface defects, some researchers have adopted the method of surface modification for SnO_2 films. For instance, a multi-fluorine-containing C_{70}-porphyrin dyad molecule $(F_{70}PD)$, bathocuproine (BCP)-core-based nonconjugated polyelectrolytes, histamine diiodate (HADI), and ionic potassium L-aspartate (PL-A) are considered suitable modification layers for the SnO_2 surface.[21–24] Their multifunctional groups can interact with surface-uncoordinated Sn^{4+} of the SnO_2 layer, enhance interfacial charge transport, and ultimately restrain carrier non-radiative recombination. Moreover, fullerene dimers prepared by combining phenanthroline with two fullerenes $(2C_{60}$-Bphen), oteracil potassium (OP), and a

[a]Key Laboratory of Functional Materials Physics and Chemistry of the Ministry of Education, Jilin Normal University, Changchun 130103, China.
E-mail: jhyang1@jlnu.edu.cn, wfy@jlnu.edu.cn, llyang1980@163.com
[b]National Demonstration Center for Experimental Physics Education, Jilin Normal University, Siping 136000, China
†Electronic supplementary information (ESI) available. See DOI: https://doi.org/10.1039/d4qi00166d

3566 | *Inorg. Chem. Front.*, 2024, **11**, 3566–3577

This journal is © the Partner Organisations 2024

potassium sulfonate salt (3Cl-BSAK) have been used to match the energy level between the SnO_2 ETL and perovskite layer, thus effectively decreasing the interface energy barrier and enhancing interfacial charge extraction.[25–27] However, the surface modification of SnO_2 films may not sufficiently passivate the bulk defects of the SnO_2 film. As a result, some researchers have focused on modifying the surface of individual SnO_2 QDs for the sake of enhancing the overall quality of SnO_2 films. Organic large molecules, such as streptomycin sulfate, heparin potassium, and poly(ethylene glycol) diacrylate, have been incorporated to significantly passivate the defects of SnO_2 QDs and inhibit their agglomeration through their multiple functional groups.[28–30] This method can result in a uniform SnO_2 film. However, the large organic molecules may induce additional steric hindrance, affecting the ETL conductivity.[31] Consequently, utilizing small ions to stabilize QDs seems to be a potential way to relax the trade-off between the surface passivation and reducing the steric hindrance.

In this study, we developed multifunctional manganese acetate $(Mn(Ac)_2)$-stabilized SnO_2 QDs (Mac-SnO_2 QDs) and utilized them to prepare ETLs for PSCs. The molecular formula of $Mn(Ac)_2$ is $(CH_3COO)_2Mn$. The $C=O$ groups of the Mac-SnO_2 QDs could terminate Sn dangling bonds, which reduces particle interactions, suppressing QDs agglomeration, and allowing forming a uniform film. Moreover, the Mac-SnO_2 QDs could reduce the defects that exist in the ETL/perovskite interface due to the $C=O$ group. Interestingly, during the experiment, we observed that the perovskite grown on Mac-SnO_2 released residual stress during annealing and the Mn^{2+} could spread upward into the perovskite layer, passivating the I^- that appear in the grain boundary. In consequence, the PCE could be elevated from 21.11% to 23.36%. More importantly, the Mac-SnO_2 devices demonstrated good long-term stability, with the PCE maintaining 90% of its original value under environmental conditions for nearly 600 h.

2. Results and discussion

In Fig. S1,† X-ray diffraction (XRD) was utilized to confirm the ETLs formation and crystallographic characteristics. The results demonstrate that the addition of $Mn(Ac)_2$ did not alter the SnO_2 crystal structure. Subsequently, the size variation between Mac-SnO_2 and SnO_2 QDs was investigated using transmission electron microscopy (TEM). The distinct electron diffraction circles observed for both samples indicated a polycrystalline nature.[32] It was found that both the SnO_2 and Mac-SnO_2 QDs had sizes of ~5 nm (Fig. 1a and b). One step further, the particle size analysis in the SnO_2 and Mac-SnO_2 colloidal dispersion was performed by dynamic light scattering (DLS) (Fig. 1c and d). The average particle sizes for the fresh SnO_2 and Mac-SnO_2 dispersions were similar, respectively. After 72 h of aging, the particle size of the fresh SnO_2 solution significantly increased, while that of the Mac-SnO_2 solution remained almost unchanged under identical conditions. Additionally, we measured the zeta potential to exhibit the electrostatic potential of the particles in solution. The fresh SnO_2 dispersion showed a zeta potential value of −23.60 mV, which declined to −9.94 mV after aging for 72 hours in storage (Fig. S2†). This indicates the electrostatic potential could not provide enough repulsion to disperse the particles, leading to unfavorable agglomeration (a common occurrence for in-
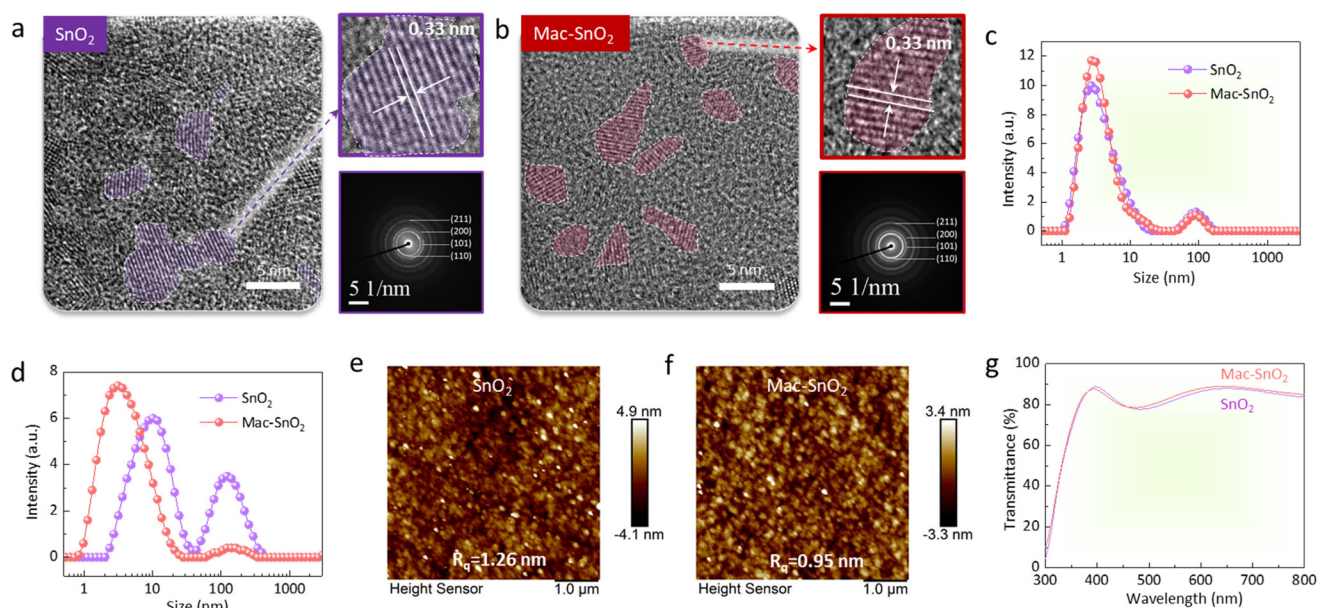

Fig. 1 HRTEM images and their SAED images of (a) SnO_2 and (b) Mac-SnO_2. (c) Particle-size distribution of fresh SnO_2 and Mac-SnO_2 solutions. (d) Particle-size distribution of 72 h-aged SnO_2 and Mac-SnO_2 solutions. AFM topographical images of (e) SnO_2 and (f) Mac-SnO_2 films. (g) Optical transmittance spectra of ITO/SnO_2 and ITO/Mac-SnO_2 films.

This journal is © the Partner Organisations 2024

Inorg. Chem. Front., 2024, **11**, 3566–3577 | **3567**

organic metal oxide particles in colloidal dispersions).[33] On the contrary, the stabilized Mac-SnO$_2$ solution exhibited a large zeta potential (−40.5 mV), and was little changed after aging, suggesting that the addition of Mn(Ac)$_2$ stabilized the SnO$_2$ QDs by terminating the surface defects, thereby inhibiting QDs agglomeration.[34] Furthermore, the more evenly dispersed Mac-SnO$_2$ particles benefit the formation of a denser and more uniform film. Top-view scanning electron microscopy (SEM) and atomic force microscopy (AFM) were carried out to illustrate the ETLs surface morphology. The Mac-SnO$_2$ film displayed a compact and dense morphology, superior to that of the SnO$_2$ film (Fig. S3†). The surface root-mean-square (R_q) roughness decreased from the SnO$_2$ film (1.26 nm) to the Mac-SnO$_2$ film (0.95 nm), manifesting the smoother film (Fig. 1e and f). Moreover, UV–visible (UV–vis) transmittance spectroscopy was performed to probe the optical properties of the SnO$_2$ and Mac-SnO$_2$ films (Fig. 1g).

The optical transmittance of the ITO/Mac-SnO$_2$ film increased in the range from 470 to 800 nm, verifying that the Mac-SnO$_2$ film was uniform and compact due to the more dispersed QDs.

In order to further elucidate the mechanism behind the differences between SnO$_2$ and Mac-SnO$_2$, we conducted a comprehensive study from various perspectives. Our findings revealed that the dispersion of SnO$_2$ was transparent and colorless, whereas the Mac-SnO$_2$ dispersion exhibited an orange hue, indicative of an interaction between Mn(Ac)$_2$ and SnO$_2$ (Fig. S4†). The interaction was analyzed through X-ray photoelectron spectroscopy (XPS) measurements (Fig. S5a†). The Mn peak of 2p could be observed in the Mac-SnO$_2$ film (Fig. S5b†). Notably, after the incorporation of Mn(Ac)$_2$, the peaks for Sn 3d$_{3/2}$ and Sn 3d$_{5/2}$ in SnO$_2$ were shifted toward lower binding energies, from 494.88 and 486.48 eV to 494.45 and 486.04 eV, respectively (Fig. 2a). This shift indicated the increased elec-
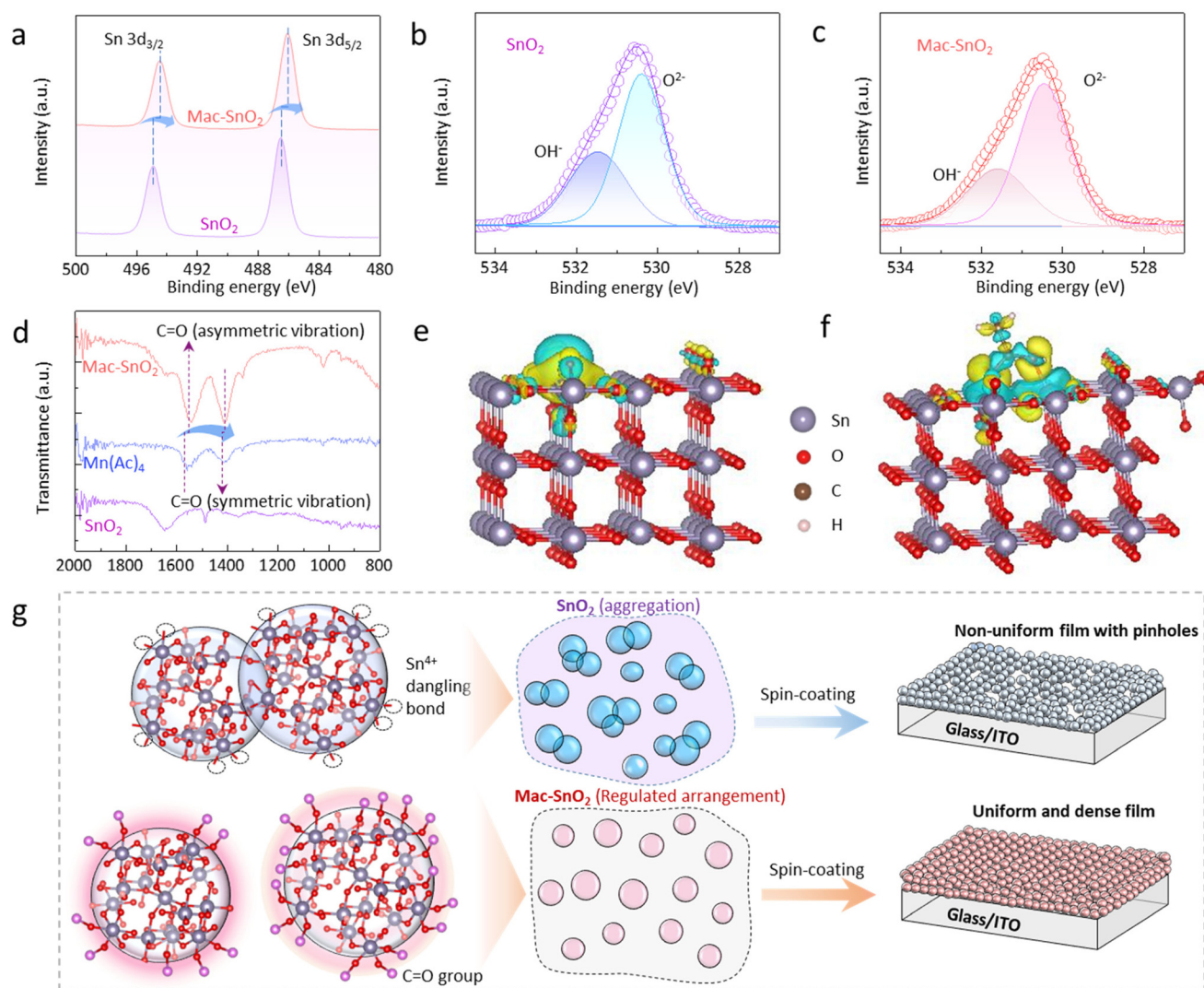

Fig. 2 XPS spectra of (a) Sn 3d and (b and c) O 1s for SnO$_2$ and Mac-SnO$_2$. (d) FTIR spectra of SnO$_2$ and Mac-SnO$_2$. Side view of (e) SnO$_2$–O$_v$ and the charge density difference of (f) SnO$_2$–O$_v$/Ac⁻. (g) Schematic of the distribution of SnO$_2$ and Mac-SnO$_2$ QDs in the solutions and films.

tron density around the Sn atoms, attributable to the interaction between Sn and $Mn(Ac)_2$.[35] Additionally, XPS for O 1s was also performed (Fig. 2b and c). The pristine SnO_2 film displayed a distinct peak at 530.38 eV, confirming the presence of hydroxyl groups (OH^-), while the peak of saturated oxygen (O^{2-}) was at 531.47 eV. However, the OH^- peak was diminished in the Mac-SnO_2 film, suggesting that C=O effectively reduced the density of absorbed OH^- sites. To further confirm the bonding between SnO_2 and $Mn(Ac)_2$, Fourier-transform infrared (FTIR) spectroscopy was conducted (Fig. 2d). $Mn(Ac)_2$ exhibited two characteristic peaks for C=O bonds.[36] After adding $Mn(Ac)_2$ into the SnO_2 QDs dispersion solution, the C=O peaks moved from 1558 and 1444 cm^{-1} to 1543 and 1412 cm^{-1}, consistent with the XPS results mentioned earlier, and further supporting the formation of Mac-SnO_2 resulting from the interaction between C=O and the SnO_2 QDs surface. This effect can reduce the following presence of OH^- groups absorbed on the oxygen vacancies and inhibit the non-radiative recombination of the SnO_2 surface, offering potential benefits.[37] We further verified our experimental results *via* density functional theory (DFT) calculations. As displayed in Fig. 2e, there were oxygen vacancies on the SnO_2 surface. After adding acetic acid groups (Ac^-), the C=O in acetic acid could combine with Sn on the SnO_2 surface (Fig. S6†). The interaction was then explored by calculating the charge density difference of Ac^- adsorbed on the SnO_2 surface (Fig. 2f). In the figure, the blue regions denote electron depletion after charge redistribution, and the yellow regions represent electron accumulation. It could be concluded that the Sn atoms obtained electrons from the C=O group through the Sn–O bond from the electron clouds at the interface, which was in accord with the XPS and FTIR results. A schematic drawing shows the whole process in Fig. 2g; whereby, the pristine SnO_2 QDs agglomerated due to a good deal of Sn^{4+} dangling bonds existing on the surface, while the C=O groups of $Mn(Ac)_2$ could passivate the Sn^{4+} dangling bonds, so that Ac^- inhibited the QDs agglomeration, like the ligands around SnO_2, thus allowing obtaining a dense Mac-SnO_2 film without pinholes.

Electrical properties are a key factor to evaluate the performance of ETLs. We determined the electrical conductivities of the two films by using the current–voltage (*I–V*) characteristic curves. The device structure of ITO/ETL/Ag was used in the test, and the specific values were as 2.81×10^{-5} S cm^{-1} (SnO_2) and 5.68×10^{-5} S cm^{-1} (Mac-SnO_2), respectively (Fig. S7a†).[38] Additionally, we obtained the electron mobility by fabricating the space charge-limited current (SCLC) model (structure: ITO/ETL/PCBM/Ag) and by using the Mott–Gurney equation (Fig. S7b†):[39]

$$\mu_e = \frac{8JL^3}{9\varepsilon_r\varepsilon_0 V^2} \quad (1)$$

where the physical quantities ε_0, ε_r, L, J, and V in the formula represent the vacuum permittivity, relative dielectric constant, ETL thickness, dark current density, and applied voltage, respectively. It was verified that the electron mobility of the

Mac-SnO_2 ETL was 5.23×10^{-3} cm^2 V^{-1} S^{-1}, which was significantly larger than that of the SnO_2 ETL (9.03×10^{-3} cm^2 V^{-1} S^{-1}). The increased conductivity and electron mobility of the Mac-SnO_2 film were ascribed to inhibited non-radiative recombination and the denser ETL film without pinholes, demonstrating the electron extraction and transfer efficiency were higher.[40]

We next investigated the surface morphology and structure of the perovskite layers based on the two types of ETLs by SEM (Fig. 3a and b). Their cross-sectional images are displayed in Fig. 3c and d. The Mac-SnO_2/perovskite grains were larger than those of the SnO_2, and the Mac-SnO_2/perovskite layer appeared denser and more uniform, while the control film exhibited undesirable pinholes. Consistent with a more homogeneous morphology, the AFM images show the R_q of the Mac-SnO_2/perovskite films (8.56 nm) was slightly reduced compared to that of the control film (9.69 nm), indicating a smoother and superior surface quality (Fig. S8†). The effect of different ETLs on the crystallization of perovskite was further explored by XRD (Fig. 3e). Two characteristic peaks at 14.0° and 28.2° were observed, indicating the (110) and (220) cubic phase of the perovskite film. Compared to the diffractions of the (110) and (220) lattice planes on the SnO_2/perovskite film, those on the Mac-SnO_2/perovskite film were stronger, which means the Mac-SnO_2/perovskite possessed enhanced crystallinity. The different crystallizations of the perovskite films may stem from the difference in the surface groups on the ETLs. We mirrored the surface Gibbs free energies *via* performing contact angle analysis of the two types of ETLs (Fig. 3f). The contact angle on Mac-SnO_2 (13.64°) was found to be lower than that on SnO_2 (22.89°), indicating the perovskite deposited on Mac-SnO_2/ETL had a lower surface Gibbs free energy and higher surface wettability.[41] Lower Gibbs free energies are beneficial for the spreading of the perovskite precursor solution, uniform nucleation, and the formation of a high-crystallinity perovskite layer.[42]

Furthermore, we conducted cross-sectional elemental mapping of the Mac-SnO_2/perovskite films (Fig. S9†), and found that Pb and I were evenly distributed within the perovskite, indicating uniform film growth. Surprisingly, we also detected the presence of Mn^{2+} in the perovskite film, suggesting that Mn^{2+} had diffused upward into the perovskite films. Previous reports indicate that Mn^{2+} can passivate I^- dangling bonds at perovskite grain boundaries, leading us to speculate that the diffused Mn^{2+} may passivate the I^- at the grain boundary.[43,44] XPS measurements were next applied to investigate the interaction between Mac-SnO_2 and the perovskite (Fig. S10†), and so $Mn(Ac)_2$ was added to the perovskite for XPS characterization. As exhibited in the I 3d spectrum (Fig. 4a), the peaks for I $3d_{5/2}$ and I $3d_{3/2}$ in the perovskite film (618.65 and 630.13 eV) moved toward higher binding energies (618.91 and 630.40 eV) after adding $Mn(Ac)_2$, which verified the Mn^{2+} and the uncoordinated I^- interact with each other, as we had estimated. Meanwhile, it could be noted that the Pb $4f_{5/2}$ and Pb $4f_{7/2}$ peaks (142.86 and 137.98 eV) were shifted to lower binding energies of 142.69 and 137.81 eV in the Mn
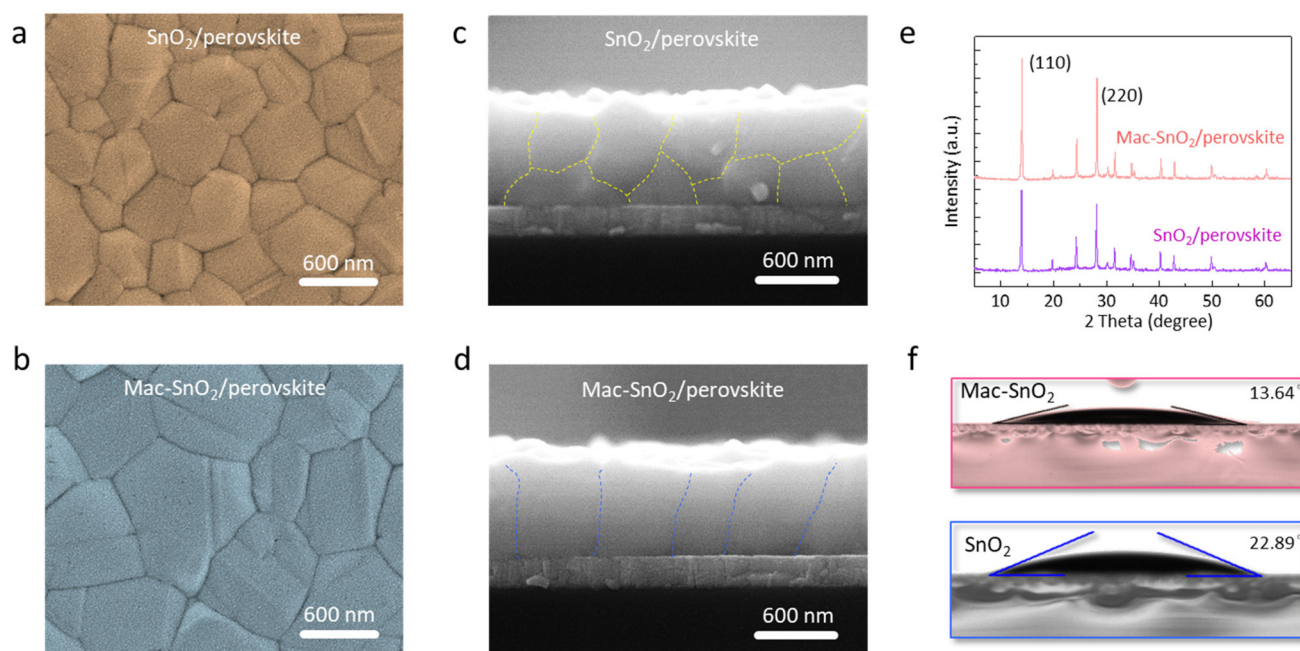
This journal is © the Partner Organisations 2024

Inorg. Chem. Front., 2024, **11**, 3566–3577 | **3569**

Fig. 3 Top-view and cross-section SEM images of perovskite layers grown on (a and c) SnO_2 and (b and d) Mac-SnO_2 ETL. (e) XRD patterns of the SnO_2/perovskite and Mac-SnO_2/perovskite. (f) The water contact angles on SnO_2 and Mac-SnO_2 films.

$(Ac)_2$-added perovskite, implying the interactions between Pb^{2+} of perovskite and the C=O of $Mn(Ac)_2$ (Fig. 4b).[45] In addition, we found a peak for Pb^0 in the perovskite sample, which disappeared in the $Mn(Ac)_2$-added perovskite sample, indicating that the interaction of Pb^{2+} dangling bonds and the C=O groups suppressed the Pb^0 production. Afterwards, we evaluated the charge trap density (N_{trap}) of the perovskite films by adopting the SCLC model (electron-only device: ITO/ETL/perovskite/PCBM/Ag) (Fig. 4c). The formula used to calculate this is as follows:[46]

$$N_{trap} = \frac{2\varepsilon\varepsilon_0 V_{TFL}}{eL^2} \tag{2}$$

where L, e, ε, and V_{TFL} represent the thickness of the perovskite films, elementary charge, relative dielectric constant of the perovskite, and the onset voltage of the trap-filled limit region, respectively. The calculated N_{trap} of the perovskite was appreciably reduced from 3.37×10^{15} (SnO_2/perovskite) to 2.27×10^{15} cm^{-3} (Mac-SnO_2/perovskite), which corresponded to the higher quality perovskite layer without pinholes and the reduced non-radiative recombination.

In addition, it is known that film stress can accelerate perovskite film degradation and device failure.[47] Consequently, we explored the residual stress of the SnO_2/perovskite and Mac-SnO_2/perovskite films by depth-dependent grazing incident X-ray diffraction (GIXRD).[48–50] Variable grazing tilt angles (ψ) from 10° to 50° were selected to detect the different depths of the perovskite films. As the incidence angle increased, the characteristic peak (110) in the SnO_2/perovskite film gradually shifted to lower angles due to the compressive stress caused by lattice contraction (Fig. 4d). On the contrary, there was a slight

peak shift for the Mac-SnO_2/perovskite film, implying a release of interfacial stress owing to the effective passivation of the uncoordinated Pb^{2+} at the perovskite buried interface (Fig. 4e).[51] Subsequently, we fitted the 2θ as a function of $\sin^2 \Psi$ to evaluate the lattice strain variation more accurately, where the slopes of the fitting line represent the residual strain and were calculated by the $2\theta - \sin^2 \Psi$ curves (Fig. 4f). Also, the elastic stress ε can be calculated as follows:[52]

$$\varepsilon = -\frac{C}{E} \cdot \frac{\partial(2\theta)}{\partial(\sin^2 \Psi)} \tag{3}$$

where C is the constant and E is the Young's modulus. The fitted curve had a negative slope in the SnO_2/perovskite film, demonstrating severe strain; while the slope was closer to 0 for the Mac-SnO_2/perovskite film, implying the residual strain was effectively eliminated. Fig. 4 g shows that the residual strain in the perovskite was significant, and there was little residual strain in the Mac-SnO_2/perovskite film.

The energy level alignment between the ETL and perovskite determines the effectiveness of charge extraction and the recombination rate. Consequently, we examined the energy level of SnO_2 and Mac-SnO_2 by ultraviolet photoelectron spectroscopy (UPS). A decreased work function (W_F) of the Mac-SnO_2 was observed, calculated to be −3.12 eV, while the value for the pristine SnO_2 was −3.16 eV (Fig. 5a and b).[53] The valence band maximum (VBM) for both were −7.90 eV (SnO_2) and −7.81 eV (Mac-SnO_2), respectively. The optical band gap (E_g) values were determined using a Tauc plot derived from the UV–vis absorption spectroscopy analysis (Fig. 5c), showing values of 3.78 eV (SnO_2) and 3.77 eV (Mac-SnO_2). The conduc-
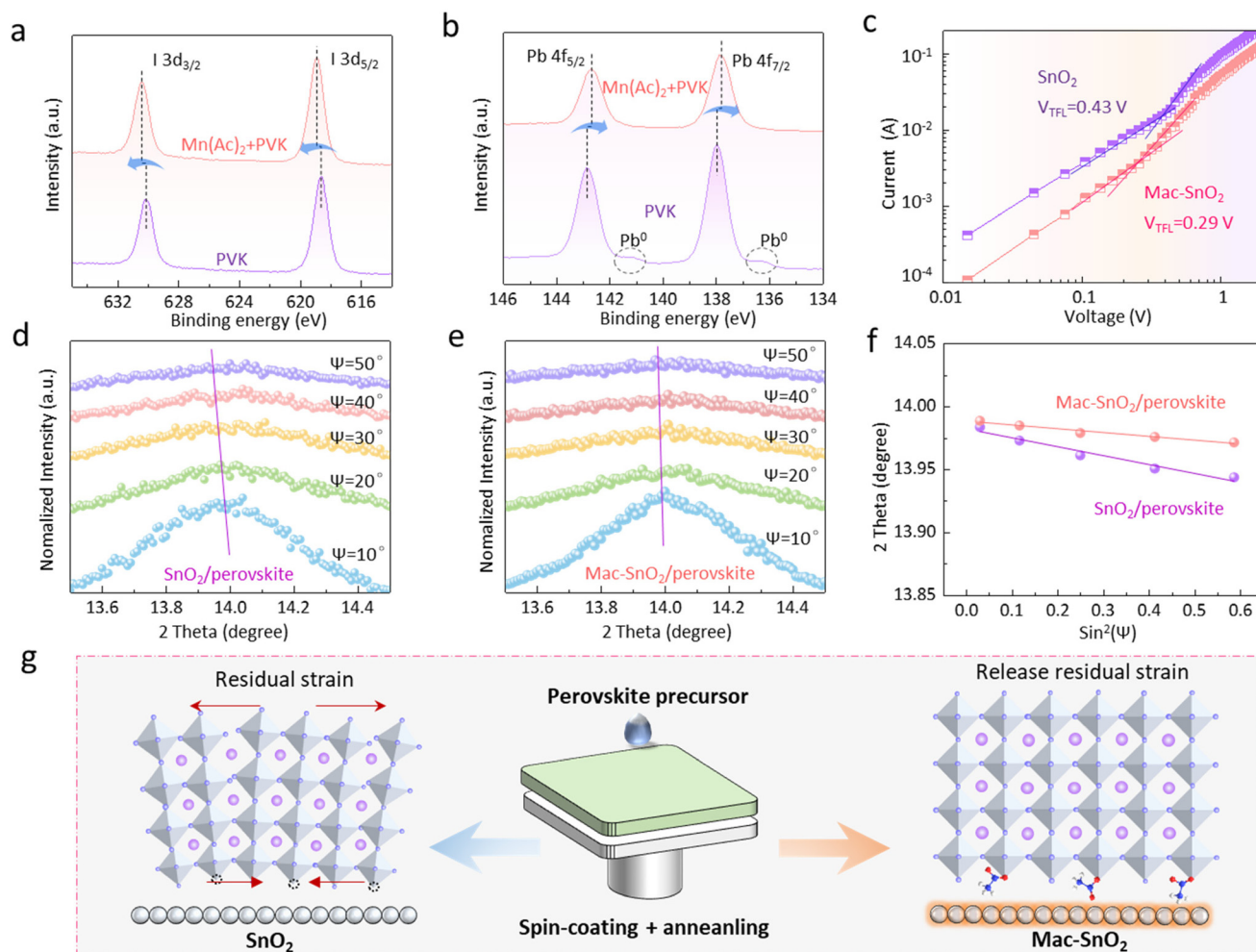
3570 | *Inorg. Chem. Front.*, 2024, **11**, 3566–3577

This journal is © the Partner Organisations 2024

Fig. 4 XPS spectra of (a) Pb 4f and (b) I 3d for the perovskite and Mn(Ac)$_2$ + perovskite. (c) Dark $I–V$ curves based on SnO$_2$ and Mac-SnO$_2$. Depth-dependent GIXRD patterns of the (d) SnO$_2$/perovskite and (e) Mac-SnO$_2$/perovskite, and their (f) linear fits of $2\theta – \sin^2 \Psi$. (g) Residual stress diagram of the SnO$_2$/perovskite and Mac-SnO$_2$/perovskite.

tion band minimum (CBM) was derived from the VBM and the E_g, and were calculated to be −4.12 eV for SnO$_2$ and −4.04 eV for Mac-SnO$_2$. The CBM of Mac-SnO$_2$ was closer to the CBM of the perovskite, resulting in a smaller energy loss during electron transfer. As displayed in Fig. 5d, the energy band diagram demonstrated that the Mac-SnO$_2$ was more beneficial for enhancing electron extraction and preventing hole transport. We further probed the surface potential of the SnO$_2$ and Mac-SnO$_2$ ETL *via* applying Kelvin probe force microscopy (KPFM) (Fig. S11†). The average surface potential of the Mac-SnO$_2$ surface (575 mV) was higher than that of the SnO$_2$ film (460 mV), which was in line with the consequences of UPS. Additionally, we examined the interfacial electron transmission processes of the control and Mac-SnO$_2$/perovskite films by measuring the steady-state photoluminescence (PL) (Fig. 5e). Significant PL quenching was noticed in the Mac-SnO$_2$/perovskite film compared to the control samples, indicating a shortened carrier recombination lifetime and enhanced electron extraction.[54] Besides the PL, in order to further

explore the carrier dynamics of the perovskite, time-resolved photoluminescence (TRPL) analysis was performed. As depicted in Fig. 5f, the Mac-SnO$_2$/perovskite film displayed a shorter lifetime in the first stage (τ_1) (10.86 ns) than that of SnO$_2$ (21.79 ns). The shortened lifetime indicated efficient charge transport at the Mac-SnO$_2$/perovskite interface due to the improved interface contact and band alignment.[55]

We fabricated complete PSCs with a structure of ITO/ETL/perovskite/HTL (Spiro-OMeTAD)/Ag to explore the influence on the device photovoltaic performance (Fig. 6a). The corresponding SEM images of devices based on the two ETLs are presented in Fig. 6b. Fig. 6c shows the reverse scanning current density–voltage ($J–V$) curve of the two champion devices. The introduction of Mac-SnO$_2$ led to a champion PCE of 23.36% [short-circuit current density (J_{sc}) = 24.96 mA cm^{-2}, open-circuit voltage (V_{oc}) = 1.16 V, fill factor (FF) = 80.69%], obviously higher than the reference PSC based on SnO$_2$ (PCE = 21.11%, J_{sc} = 24.25 mA cm^{-2}, V_{oc} = 1.12 V, FF = 77.66%). The photovoltaic parameters of the forward scans are shown in

This journal is © the Partner Organisations 2024

Inorg. Chem. Front., 2024, **11**, 3566–3577 | **3571**
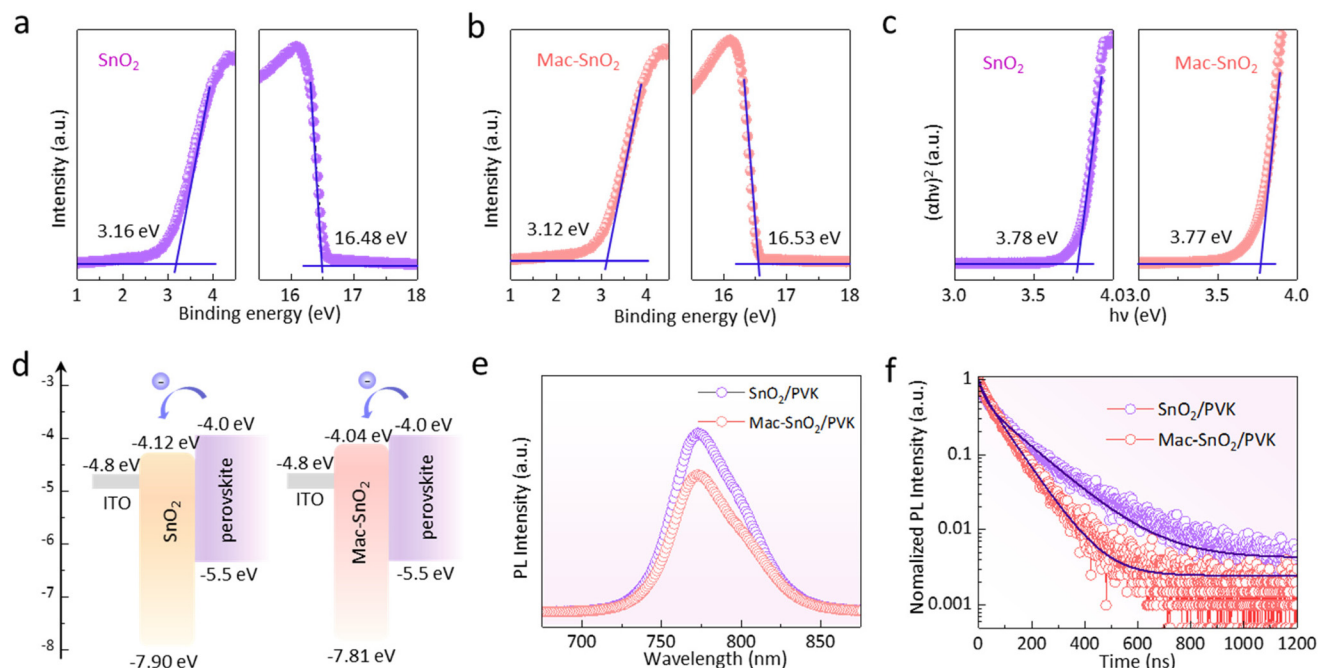
Fig. 5 UPS spectra of (a) SnO$_2$ and (b) Mac-SnO$_2$. (c) Tauc plots of SnO$_2$ (left) and Mac-SnO$_2$ (right). (d) Energy band structure diagram of the ETL and perovskite. (e) PL and (f) TRPL spectra of perovskite layers deposited on glass/SnO$_2$ and glass/Mac-SnO$_2$ substrates.
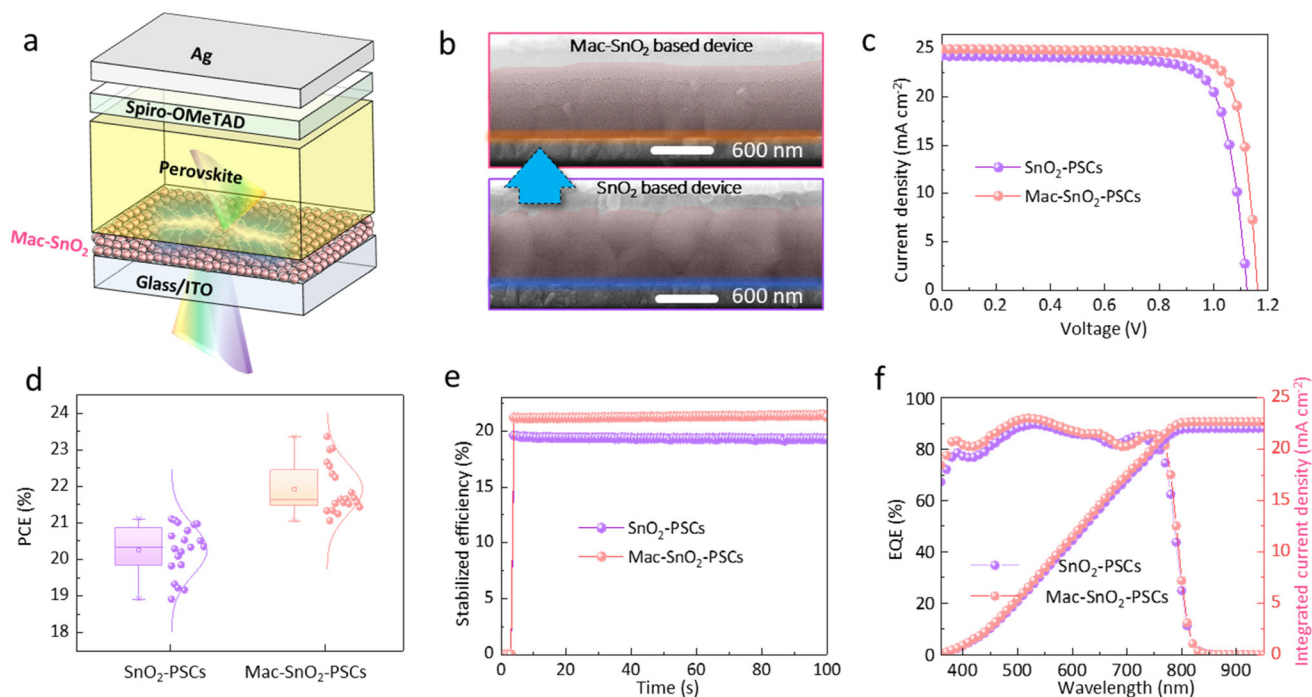

Fig. 6 (a) Schematic structure of a Mac-SnO$_2$-based PSC. (b) SEM images of the cross-sections of the SnO$_2$- and Mac-SnO$_2$-based devices. (c) J–V curves of the optimal SnO$_2$ and Mac-SnO$_2$ cells. (d) PCE distributions of the SnO$_2$- and Mac-SnO$_2$-based devices from 20-device statistics, respectively. (e) Steady-state output of the SnO$_2$ and Mac-SnO$_2$ PSCs measured at MPP. (f) EQE spectra of the SnO$_2$- and Mac-SnO$_2$-based devices.

Table S1.† The V_{oc} and FF displayed significant improvements, which could be mainly ascribed to the reduced bulk and interfacial non-radiative recombination, and the suitable energy band alignment of the Mac-SnO$_2$/perovskite film, leading to rapid charge carrier extraction. Compared with the pristine sample, the PSC devices based on Mac-SnO$_2$ demonstrated

3572 | *Inorg. Chem. Front.*, 2024, **11**, 3566–3577

This journal is © the Partner Organisations 2024

lower hysteresis, which was likely due to the efficient carrier transport and reduced non-radiative recombination (Fig. S12†). Furthermore, we varied the concentrations of the Mac-SnO$_2$ solution to determine the optimal PCE (Fig. S13†). The relevant parameters are exhibited in Table S2,† indicating that the best PCE was obtained when the Mn(Ac)$_2$ concentration was 7.5 mg mL^{-1}. Subsequently, we fabricated 20 individual devices based on the SnO$_2$ and the optimized Mac-SnO$_2$ layers. The statistical histogram of the PCEs and other parameters are displayed in Fig. 6d, and Tables S3 and S4.† Based on the parameters, it could be concluded that the devices based on different ETLs all exhibited excellent reproducibility, with the Mac-SnO$_2$ ETL devices showing higher PCEs. A comparative analysis of the maximum power point (MPP) was conducted to understand the steady PCE outputs and PCEs for SnO$_2$ and Mac-SnO$_2$ devices, respectively (Fig. 6e). The Mac-SnO$_2$ device exhibited a stable PCE of 21.61% over 100 s, which the J–V results above accorded with. Meanwhile, the SnO$_2$ device demonstrated a stable PCE of 19.51% over time, indicating that devices with Mac-SnO$_2$ ETLs offered greater operational stability. The external quantum efficiency (EQE) spectra of the PSCs and the integrated current density curve are exhibited in Fig. 6f, while the EQE spectra of cells with different Mac-SnO$_2$ concentrations are shown in Fig. S14.†

The performance of cells is closely associated with the trap-assisted recombination behavior. We performed light intensity-dependent V_{oc} analysis to gain insights into the mechanism of the carrier recombination process (Fig. S15a†). The relationship where V_{oc} is dependent on the light intensity is as follows:[56]

$$V_{oc} = \frac{nkT \ln(I)}{q} + \text{constant} \tag{4}$$

where n, k, and I represent the ideal coefficient, Boltzmann constant, and light intensity, respectively. Compared to the n value of 1.36 for PSCs with pristine SnO$_2$, the lower n value for the Mac-SnO$_2$ device (1.12) indicated that trap-assisted Shockley–Read–Hall (SRH) monomolecular recombination was inhibited. Meanwhile, the light intensity-dependent J_{sc} analysis was performed (Fig. S15b†). In general, the expression J_{sc}

$\propto I^\alpha$ describes the relationship of the J_{sc} with the light intensity.[57] The α of the Mac-SnO$_2$ PSC (0.99) was closer to 1 compared to the pristine SnO$_2$ device (0.98), which indicated the negligible bimolecular recombination of the Mac-SnO$_2$ device. The recombination rates of PSCs were also explored by conducting transient photovoltage (TPV) measurements (Fig. S16†). The Mac-SnO$_2$ device demonstrated a longer lifetime (263 μs), while that of the SnO$_2$ device was 126 μs. The slower carrier recombination was attributed to the reduced trap-assisted recombination, leading to the higher V_{oc} in the Mac-SnO$_2$ devices.[58] Furthermore, carrier migration owing to defects in PSCs will result in the formation of dark current. The Mac-SnO$_2$ devices displayed a lower leakage current, indicating inhibited non-radiative recombination at the interface (Fig. S17†).[59] Subsequently, electrochemical impedance spectroscopy (EIS) measurements were utilized to explore the carrier recombination and carrier-transport behaviors in the two types of devices (Fig. S18†). It is well known that the high-frequency ranges in a Nyquist diagram is associated with transfer resistance (R_{tr}) at the ETL/perovskite interface, and the high frequency represents the recombination resistance (R_{rec}).[60] The Mac-SnO$_2$ devices exhibited a relatively lower R_{tr} value but higher R_{rec} value than that of the control devices, demonstrating a low electron-transfer barrier and restrained recombination at the interfaces. The built-in potential (V_{bi}) and the carrier-transport behavior of PSCs can be estimated via capacitance–voltage (C–V) measurements (Fig. S19†). The extracted V_{bi} values of the SnO$_2$ and Mac-SnO$_2$ devices were approximately 0.95 and 1.07 V, respectively. A higher V_{bi} is conducive to extending the depletion region to increase the driving force for photogenerated carriers and accelerate carrier transport, which were in accordance with the V_{oc} values for the PSCs.[61] The above discussions of the PSCs shows that the Mac-SnO$_2$ ETL could effectively improve the interface electron transfer and suppress non-radiative recombination.

Besides the photovoltaic properties, the stability of cells is also crucial for practical applications. Consequently, the long-term stability of the two cells under the ambient environment (25–30 °C, 30%–40% humidity) was monitored. As depicted in Fig. 7a, the Mac-SnO$_2$ PSC possessed an increased life. After
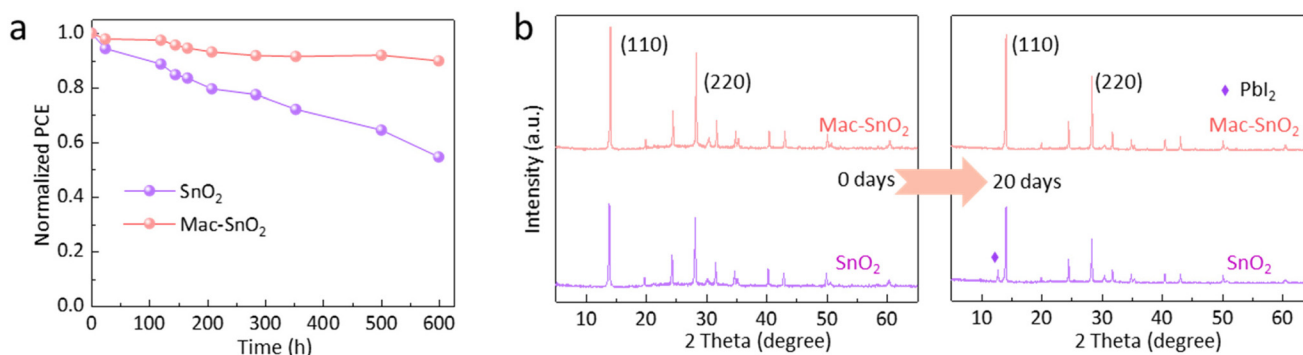

Fig. 7 (a) Normalized PCEs of SnO$_2$ and Mac-SnO$_2$ PSCs placed in the ambient environment (25–30 °C, 30%–40% humidity). (b) XRD spectra of the SnO$_2$/perovskite and Mac-SnO$_2$/perovskite before and after exposure to an air environment with 30%–40% humidity for 20 days.

This journal is © the Partner Organisations 2024

Inorg. Chem. Front., 2024, 11, 3566–3577 | 3573

storage for 600 h, the Mac-SnO$_2$-based PSCs maintained 90% of the initial PCE, whereas the SnO$_2$ PSC degraded faster, dropping to 55% of its initial efficiency. Moreover, the XRD patterns of the SnO$_2$/perovskite film exhibited a clear peak of PbI$_2$ after 20 days under ambient conditions (Fig. 7b). It was also observed that part of the SnO$_2$/perovskite film changed color from black to yellow, while the Mac-SnO$_2$/perovskite film maintained a well-preserved structure and black color (Fig. S20†). We also tested the light stability and thermal stability of devices. After storing the device in a N$_2$ atmosphere at 85 °C for 150 h, the efficiency of the Mac-SnO$_2$ device retained 84% of its original PCE, while the SnO$_2$ device quickly dropped to 59% of its original PCE (Fig. S21a†). In addition, after lighting the devices continuously for 60 h under 1 sun illumination, the Mac-SnO$_2$-based device retained 78% of the original PCE, while the SnO$_2$-based device retained only 61% of the original efficiency (Fig. S21b†). Consequently, the introduction of Mac-SnO$_2$ proved to be an efficient way to improve the stability of the device.

3. Conclusion

In summary, we developed multifunctional Mac-SnO$_2$ QDs and employed them to fabricate ETLs for PSCs. The C=O groups in Mn(Ac)$_2$ could passivate the Sn^{4+} on the surface of the SnO$_2$ QDs, thereby reducing the van der Waals forces between the QDs, inhibiting QDs agglomeration, and contributing to the increased conductivity of the Mac-SnO$_2$ ETLs. Meanwhile, the Mn^{2+} spread upward in the perovskite layer, passivating the I$^-$ at the grain boundary and reducing perovskite bulk defects. The perovskite grown on the Mac-SnO$_2$ ETL could release residual stress and suppress non-radiative recombination at the interface. Moreover, the well-matched energy level between Mac-SnO$_2$ and the perovskite is beneficial for extracting and transporting electrons. Ultimately, the champion device showed an increased PCE from 21.11% to 23.36%. More importantly, the Mac-SnO$_2$ devices also displayed enhanced long-term stability, with the PCE maintaining 90% of the original value under environmental conditions for nearly 600 h. Therefore, using multifunctional organic acid salts to stabilize SnO$_2$ QDs offers an effective method to further improve ETL quality and PSC performance. In the future, we should further explore small ions with better passivation effects and smaller resistance to stabilize SnO$_2$ QDs, which will further enhance the conductivity of the ETL. In addition, the use of ionic liquids to stabilize SnO$_2$ QDs is also a method worth exploring in depth, as it can not only passivate the surface defects of QDs, but also effectively inhibit ion migration at the ETL/perovskite interface through organic ligands, thereby improving device performance and stability.

4. Experimental section

Preparation of the ETL

The SnO$_2$ colloidal dispersion was diluted with deionized water at a ratio of 1 : 3. In the case of the Mac-SnO$_2$ solution, different concentrations of Mn(Ac)$_2$ (2.5, 5.0, 7.5, 10.0, and 12.5 mg mL^{-1} in deionized water) were added to the SnO2 colloid dispersion, also at a ratio of 1 : 3.

Fabrication of the PSCs

The ITO substrate needed to undergo washing four times with deionized water and alcohol, respectively, with each cycle requiring 20 min of ultrasonic treatment. Subsequently, the ITO substrates were treated with a 20 min exposure to ultra-violet ozone (UV/O$_3$). The SnO$_2$ solution and Mac-SnO$_2$ solution were spin-coated on the ITO substrate at 3000 rpm for 30 s, then annealed at 150 °C for half an hour and then cooled to room temperature. The ITO/ETL samples were further subjected to a 20 min UV/O$_3$ treatment. Next, in order to grow the perovskite layer, the ITO/ETL material was transferred into a nitrogen-filled glove box (with H$_2$O and O$_2$ concentrations of <1 ppm). In the case of the perovskite solution, it was formed by dissolving 217 mg of FAI (1.26 mmol), 643 mg of PbI$_2$ (1.39 mmol), 27 mg of PbBr, 19 mg of CsI, 7.4 mg of MABr, and 20 mg of MACl in 1 mL mixed solvent (DMSO to DMF volume ratio of 2 : 8). A total of 85 μL of the Cs$_{0.05}$(FA$_{0.85}$MA$_{0.15}$)$_{0.95}$Pb(I$_{0.85}$Br$_{0.15}$)$_3$ precursor solution was then deposited onto the ITO/SnO$_2$ layer using a spin-coating process of 10 s at 1000 rpm and 30 s at 5000 rpm. At 27 s after the start of the procedure, 120 μL of CB was injected onto the rotating substrate for 2 s. The resulting films were heated for 1 h at 100 °C. Subsequently, to produce the HTL mixed solution, 72.3 mg of Spiro-OMeTAD was combined with 35 μL of Li-TFSI solution (250 mg of Li-TFSI in 1 mL of acetonitrile), 10 μL of FK209 solution (300 mg of FK209 in 1 mL of acetonitrile), and 30 μL of TBP in 1 mL of CB. Next, 85 μL of the HTL mixture was spin-coated onto the perovskite films for 30 s at 4000 rpm. The final step involved plating a 100 nm Ag layer under vacuum conditions.

For more comprehensive information regarding the materials used and the characterization processes, refer to ESI notes 1 and 2.†

Conflicts of interest

There are no conflicts to declare.

Acknowledgements

References

1 T. Kim, S. Park, V. Iyer, B. Shaheen, U. Choudhry, Q. Jiang, G. Eichman, R. Gnabasik, K. Kelley, B. Lawrie, K. Zhu and

3574 | *Inorg. Chem. Front.*, 2024, **11**, 3566–3577

This journal is © the Partner Organisations 2024

B. Liao, Mapping the pathways of photo-induced ion migration in organic-inorganic hybrid halide perovskites, *Nat. Commun.*, 2023, **14**, 1846.

2 Y. Luo, R. K. Chitumalla, S.-Y. Ham, D. N. Cakan, T. Kim, S. Paek, Y. S. Meng, J. Jang, D. P. Fenning and M.-c. Kim, A Si-Substituted Spirobifluorene Hole-Transporting Material for Perovskite Solar Cells, *ACS Energy Lett.*, 2023, **8**, 5003–5011.

3 W. Zhao, M. Wu, Z. Liu, S. Yang, Y. Li, J. Wang, L. Yang, Y. Han and S. Liu, Orientation Engineering via 2D Seeding for Stable 24.83% Efficiency Perovskite Solar Cells, *Adv. Energy Mater.*, 2023, **13**, 2204260.

4 M. Kim, J. Jeong, H. Lu, T. K. Lee, F. T. Eickemeyer, Y. Liu, I. W. Choi, S. J. Choi, Y. Jo, H.-B. Kim, S.-I. Mo, Y.-K. Kim, H. Lee, N. G. An, S. Cho, W. R. Tress, S. M. Zakeeruddin, A. Hagfeldt, J. Y. Kim, M. Grätzel and D. S. Kim, Conformal quantum dot–SnO$_2$ layers as electron transporters for efficient perovskite solar cells, *Science*, 2022, **375**, 302–306.

5 J. Park, J. Kim, H.-S. Yun, M. J. Paik, E. Noh, H. J. Mun, M. G. Kim, T. J. Shin and S. I. Seok, Controlled growth of perovskite layers with volatile alkylammonium chlorides, *Nature*, 2023, **616**, 724–730.

6 Best Research-Cell Efficiency Chart, Photovolataic Research NREL, **https://ww.nrel.gov/pv/cell-effcency.html**.

7 T. Zhang, Q. He, J. Yu, A. Chen, Z. Zhang and J. Pan, Recent progress in improving strategies of inorganic electron transport layers for perovskite solar cells, *Nano Energy*, 2022, **104**, 107918.

8 W. Zhao, P. Guo, C. Liu, N. Jia, Z. Fang, L. Ye, Q. Ye, Y. Xu, A. P. Glotov, A. A. Novikov, V. A. Vinokurov, D. Harvey, D. Shchukin and H. Wang, Laser Derived Electron Transport Layers with Embedded p-n Heterointerfaces Enabling Planar Perovskite Solar Cells with Efficiency over 25, *Adv. Mater.*, 2023, **35**, e2300403.

9 A. Culu, I. C. Kaya and S. Sonmezoglu, Spray-Pyrolyzed Tantalium-Doped TiO$_2$ Compact Electron Transport Layer for UV-Photostable Planar Perovskite Solar Cells Exceeding 20% Efficiency, *ACS Appl. Energy Mater.*, 2022, **5**, 3454–3462.

10 Ö. Ateş Sönmezoğlu, S. Akın, B. Terzi, S. Mutlu and S. Sönmezoğlu, An Effective Approach for High-Efficiency Photoelectrochemical Solar Cells by Using Bifunctional DNA Molecules Modified Photoanode, *Adv. Funct. Mater.*, 2016, **26**, 8776–8783.

11 D. Wang, X. Guo, G. Zhang, Y. Liu, S. Liu, Z. Zhang, Y. Chai, Y. Chen, J. Zhang and B. Sun, SnO$_2$ electron transport layer modified by F/N-doped graphdiyne and in situ XRD and in situ XAFS exploration on its effect on perovskite active layer, *Nano Today*, 2023, **50**, 101852.

12 P. Chen, W. Pan, S. Zhu, F. Cao, A. Tong, R. He, Z. Lan, W. Sun and J. Wu, Buried modification with tetramethylammonium chloride to enhance the performance of perovskite solar cells with n-i-p structure, *Chem. Eng. J.*, 2023, **468**, 143652.

13 Y. Wang, M. Feng, H. Chen, M. Ren, H. Wang, Y. Miao, Y. Chen and Y. Zhao, Highly Crystalized Cl–Doped SnO$_2$ Nanocrystals for Stable Aqueous Dispersion Toward High–Performance Perovskite Photovoltaics, *Adv. Mater.*, 2023, **36**, 202305849.

14 D. Yang, R. Yang, C. Zhang, T. Ye, K. Wang, Y. Hou, L. Zheng, S. Priya and S. Liu, Highest–Efficiency Flexible Perovskite Solar Module by Interface Engineering for Efficient Charge–Transfer, *Adv. Mater.*, 2023, **35**, 2302484.

15 S. Sonmezoglu and S. Akin, Suppression of the interface-dependent nonradiative recombination by using 2-methyl-benzimidazole as interlayer for highly efficient and stable perovskite solar cells, *Nano Energy*, 2020, **76**, 105127.

16 Z. Li, C. Wang, P.-P. Sun, Z. Zhang, Q. Zhou, Y. Du, J. Xu, Y. Chen, Q. Xiong, L. Ding, M. K. Nazeeruddin and P. Gao, In-situ peptization of WO$_3$ in alkaline SnO$_2$ colloid for stable perovskite solar cells with record fill-factor approaching the shockley–queisser limit, *Nano Energy*, 2022, **100**, 107468.

17 W. Dong, C. Zhu, C. Bai, Y. Ma, L. Lv, J. Zhao, F. Huang, Y. B. Cheng and J. Zhong, Low–Cost Hydroxyacid Potassium Synergists as an Efficient In Situ Defect Passivator for High Performance Tin–Oxide–Based Perovskite Solar Cells, *Angew. Chem., Int. Ed.*, 2023, **62**, e202302507.

18 J. Fu, J. Zhang, T. Zhang, L. Yuan, Z. Zhang, Z. Jiang, Z. Huang, T. Wu, K. Yan, L. Zhang, A. Wang, W. Ji, Y. Zhou and B. Song, Synergistic Effects of Interfacial Energy Level Regulation and Stress Relaxation via a Buried Interface for Highly Efficient Perovskite Solar Cells, *ACS Nano*, 2023, **17**, 2802–2812.

19 H. Zhou, L. Yang, Y. Duan, M. Wu, Y. Li, D. Xu, H. Zou, J. Wang, S. Yang and Z. Liu, 24.96%-Efficiency FACsPbI$_3$ Perovskite Solar Cells Enabled by an Asymmetric 1,3-Thiazole-2,4-Diammonium, *Adv. Energy Mater.*, 2023, **13**, 2204372.

20 Y.-C. Ye, L. Chen, X.-M. Chen, C.-Y. Ma, B.-H. Lv, J.-Y. Wang, W.-D. Dou, C. Zhang, T.-L. Ma and J.-X. Tang, Interfacial Energy Level Alignment and Defect Passivation by Using a Multifunctional Molecular for Efficient and Stable Perovskite Solar Cells, *Adv. Funct. Mater.*, 2023, 2310136.

21 P. Song, E. Hou, Y. Liang, J. Luo, L. Xie, J. Qiu, C. Tian and Z. Wei, Regulating Orientational Crystallization and Buried Interface for Efficient Perovskite Solar Cells Enabled by a Multi–Fluorine–Containing Higher Fullerene Derivative, *Adv. Funct. Mater.*, 2023, **33**, 2303841.

22 J. H. Kim, Y. R. Kim, J. Kim, C. M. Oh, I. W. Hwang, J. Kim, S. Zeiske, T. Ki, S. Kwon, H. Kim, A. Armin, H. Suh and K. Lee, Efficient and Stable Perovskite Solar Cells with a High Open–Circuit Voltage Over 1.2 V Achieved by a Dual–Side Passivation Layer, *Adv. Mater.*, 2022, **34**, 2205268.

23 L. Yang, J. Feng, Z. Liu, Y. Duan, S. Zhan, S. Yang, K. He, Y. Li, Y. Zhou, N. Yuan, J. Ding and S. Liu, Record–Efficiency Flexible Perovskite Solar Cells Enabled by Multifunctional Organic Ions Interface Passivation, *Adv. Mater.*, 2022, **34**, 2201681.

This journal is © the Partner Organisations 2024

Inorg. Chem. Front., 2024, **11**, 3566–3577 | **3575**

24 L. Wang, J. Xia, Z. Yan, P. Song, C. Zhen, X. Jiang, G. Shao, Z. Qiu, Z. Wei, J. Qiu and M. K. Nazeeruddin, Robust Interfacial Modifier for Efficient Perovskite Solar Cells: Reconstruction of Energy Alignment at Buried Interface by Self–Diffusion of Dopants, *Adv. Funct. Mater.*, 2022, **32**, 2204725.

25 X. Yu, Q. Zhou, T. Zheng, R. Peng, B. Fan, L. Fan and B. Jin, Interface engineering for achieving efficient and stable perovskite solar cells by Bphen-fullerene dimer, *Chem. Eng. J.*, 2023, **452**, 139412.

26 H. Bi, Y. Guo, M. Guo, C. Ding, S. Hayase, T. Mou, Q. Shen, G. Han and W. Hou, Highly efficient and low hysteresis methylammonium-free perovskite solar cells based on multifunctional oteracil potassium interface modification, *Chem. Eng. J.*, 2022, **439**, 135671.

27 Y. Dong, W. Shen, W. Dong, C. Bai, J. Zhao, Y. Zhou, F. Huang, Y. B. Cheng and J. Zhong, Chlorobenzenesulfonic Potassium Salts as the Efficient Multifunctional Passivator for the Buried Interface in Regular Perovskite Solar Cells, *Adv. Energy Mater.*, 2022, **12**, 2200417.

28 T. Yan, C. Zhang, S. Li, Y. Wu, Q. Sun, Y. Cui and Y. Hao, Multifunctional Aminoglycoside Antibiotics Modified SnO_2 Enabling High Efficiency and Mechanical Stability Perovskite Solar Cells, *Adv. Funct. Mater.*, 2023, **33**, 2302336.

29 Z. Xiong, L. Lan, Y. Wang, C. Lu, S. Qin, S. Chen, L. Zhou, C. Zhu, S. Li, L. Meng, K. Sun and Y. Li, Multifunctional Polymer Framework Modified SnO_2 Enabling a Photostable α-$FAPbI_3$ Perovskite Solar Cell with Efficiency Exceeding 23%, *ACS Energy Lett.*, 2021, **6**, 3824–3830.

30 S. You, H. Zeng, Z. Ku, X. Wang, Z. Wang, Y. Rong, Y. Zhao, X. Zheng, L. Luo, L. Li, S. Zhang, M. Li, X. Gao and X. Li, Multifunctional Polymer–Regulated SnO_2 Nanocrystals Enhance Interface Contact for Efficient and Stable Planar Perovskite Solar Cells, *Adv. Mater.*, 2020, **32**, 2003990.

31 D. Zheng, R. Peng, G. Wang, J. L. Logsdon, B. Wang, X. Hu, Y. Chen, V. P. Dravid, M. R. Wasielewski, J. Yu, W. Huang, Z. Ge, T. J. Marks and A. Facchetti, Simultaneous Bottom–Up Interfacial and Bulk Defect Passivation in Highly Efficient Planar Perovskite Solar Cells using Nonconjugated Small–Molecule Electrolytes, *Adv. Mater.*, 2019, **31**, 1970283.

32 P. Wang, B. Chen, R. Li, S. Wang, N. Ren, Y. Li, S. Mazumdar, B. Shi, Y. Zhao and X. Zhang, Cobalt Chloride Hexahydrate Assisted in Reducing Energy Loss in Perovskite Solar Cells with Record Open-Circuit Voltage of 1.20 V, *ACS Energy Lett.*, 2021, **6**, 2121–2128.

33 L. Zhang, C. Fu, S. Wang, M. Wang, R. Wang, S. Xiang, Z. Wang, J. Liu, H. Ma, Y. Wang, Y. Yan, M. Chen, L. Shi, Q. Dong, J. Bian and Y. Shi, Amorphous F–doped TiO_x Caulked SnO_2 Electron Transport Layer for Flexible Perovskite Solar Cells with Efficiency Exceeding 22.5%, *Adv. Funct. Mater.*, 2023, **33**, 2213961.

34 L. Chen, Z. Liu, L. Qiu, J. Xiong, L. Song and P. Du, Multifunctional Regulation of SnO_2 Nanocrystals by Snail

Mucus for Preparation of Rigid or Flexible Perovskite Solar Cells in Air, *ACS Nano*, 2023, **17**, 23794–23804.

35 X. Ji, L. Bi, Q. Fu, B. Li, J. Wang, S. Y. Jeong, K. Feng, S. Ma, Q. Liao, F. R. Lin, H. Y. Woo, L. Lu, A. K. Y. Jen and X. Guo, Target Therapy for Buried Interface Enables Stable Perovskite Solar Cells with 25.05% Efficiency, *Adv. Mater.*, 2023, **35**, 2303665.

36 Y. Zhang, T. Kong, H. Xie, J. Song, Y. Li, Y. Ai, Y. Han and D. Bi, Molecularly Tailored SnO_2/Perovskite Interface Enabling Efficient and Stable $FAPbI_3$ Solar Cells, *ACS Energy Lett.*, 2022, **7**, 929–938.

37 R. Zhao, Z. Deng, Z. Zhang, J. Zhang, T. Guo, Y. Xing, X. Liu, L. Huang, Z. Hu and Y. Zhu, Alkali Metal Cations Modulate the Energy Level of SnO_2 via Micro-agglomerating and Anchoring for Perovskite Solar Cells, *ACS Appl. Mater. Interfaces*, 2022, **14**, 36711–36720.

38 J. Zhuang, P. Mao, Y. Luan, N. Chen, X. Cao, G. Niu, F. Jia, F. Wang, S. Cao and J. Wang, Rubidium Fluoride Modified SnO_2 for Planar n-i-p Perovskite Solar Cells, *Adv. Funct. Mater.*, 2021, **31**, 2010385.

39 Y. Li, S. Li, Y. Shen, X. Han, Y. Li, Y. Yu, M. Huang and X. Tao, Multifunctional Histidine Cross-Linked Interface toward Efficient Planar Perovskite Solar Cells, *ACS Appl. Mater. Interfaces*, 2022, **14**, 47872–47881.

40 Y. Chen, X. Zuo, Y. He, F. Qian, S. Zuo, Y. Zhang, L. Liang, Z. Chen, K. Zhao, Z. Liu, J. Gou and S. Liu, Dual Passivation of Perovskite and SnO_2 for High–Efficiency $MAPbI_3$ Perovskite Solar Cells, *Adv. Sci.*, 2021, **8**, 2001466.

41 Z. Lv, L. He, H. Jiang, X. Ma, F. Wang, L. Fan, M. Wei, J. Yang, L. Yang and N. Yang, Diluted-CdS Quantum Dot-Assisted SnO_2 Electron Transport Layer with Excellent Conductivity and Suitable Band Alignment for High-Performance Planar Perovskite Solar Cells, *ACS Appl. Mater. Interfaces*, 2021, **13**, 16326–16335.

42 M. Wu, Y. Duan, L. Yang, P. You, Z. Li, J. Wang, H. Zhou, S. Yang, D. Xu, H. Zou and Z. Liu, Multifunctional Small Molecule as Buried Interface Passivator for Efficient Planar Perovskite Solar Cells, *Adv. Funct. Mater.*, 2023, **33**, 2300128.

43 W. Liu, L. Chu, N. Liu, Y. Ma, R. Hu, Y. Weng, H. Li, J. Zhang, X. a. Li and W. Huang, Efficient perovskite solar cells fabricated by manganese cations incorporated in hybrid perovskites, *J. Mater. Chem. C*, 2019, **7**, 11943–11952.

44 G. Tong, L. K. Ono, Y. Liu, H. Zhang, T. Bu and Y. Qi, Up-Scalable Fabrication of SnO_2 with Multifunctional Interface for High Performance Perovskite Solar Modules, *Nano-Micro Lett.*, 2021, **13**, 15.

45 Z. Wang, S. You, G. Zheng, Z. Tang, L. Zhang, J. Zhang, X. Li and X. Gao, Tartaric acid additive to enhance perovskite multiple preferential orientations for high-performance solar cells, *J. Energy Chem.*, 2022, **69**, 406–413.

46 T. Li, S. Wang, J. Yang, X. Pu, B. Gao, Z. He, Q. Cao, J. Han and X. Li, Multiple functional groups synergistically improve the performance of inverted plannar perovskite solar cells, *Nano Energy*, 2021, **82**, 105742.

47 Y. Meng, C. Liu, R. Cao, J. Zhang, L. Xie, M. Yang, L. Xie, Y. Wang, X. Yin, C. Liu and Z. Ge, Pre-Buried ETL with Bottom-Up Strategy Toward Flexible Perovskite Solar Cells with Efficiency Over 23%, *Adv. Funct. Mater.*, 2023, **33**, 2214788.

48 S. Sönmezoğlu, T. A. Termeli, S. Akın and İ. Askeroğlu, Synthesis and characterization of tellurium-doped CdO nanoparticles thin films by sol–gel method, *J. Sol-Gel Sci. Technol.*, 2013, **67**, 97–104.

49 S. Akın, G. Karanfil, A. Gültekin and S. Sönmezoğlu, Improvement of physical properties of CdO thin films by Au–Ag nanocluster codoping, *J. Alloys Compd.*, 2013, **579**, 272–278.

50 O. Altintas Yildirim, H. Arslan and S. Sönmezoğlu, Facile synthesis of cobalt-doped zinc oxide thin films for highly efficient visible light photocatalysts, *Appl. Surf. Sci.*, 2016, **390**, 111–121.

51 B. Liu, H. Bi, D. He, L. Bai, W. Wang, H. Yuan, Q. Song, P. Su, Z. Zang, T. Zhou and J. Chen, Interfacial Defect Passivation and Stress Release via Multi-Active-Site Ligand Anchoring Enables Efficient and Stable Methylammonium-Free Perovskite Solar Cells, *ACS Energy Lett.*, 2021, **6**, 2526–2538.

52 J. Wu, Y. Cui, B. Yu, K. Liu, Y. Li, H. Li, J. Shi, H. Wu, Y. Luo, D. Li and Q. Meng, A Simple Way to Simultaneously Release the Interface Stress and Realize the Inner Encapsulation for Highly Efficient and Stable Perovskite Solar Cells, *Adv. Funct. Mater.*, 2019, **29**, 1905336.

53 Z. Wu, J. Wu, S. Wang, C. Wang, Y. Du, Y. Wang, J. Geng, Y. Lin, W. Sun and Z. Lan, Multifunctional molecule of potassium nonafluoro-1-butanesulfonate for high-efficient perovskite solar cells, *Chem. Eng. J.*, 2022, **449**, 137851.

54 F. Fei, L. Gu, Y. Xu, K. Du, X. Zhou, X. Dong, X. Chen, N. Yuan, S. Wang and J. Ding, Method to Inhibit Perovskite Solution Aging: Induced by Perovskite Microcrystals, *ACS Appl. Mater. Interfaces*, 2022, **14**, 52960–52970.

55 W. Zhao, P. Guo, J. Su, Z. Fang, N. Jia, C. Liu, L. Ye, Q. Ye, J. Chang and H. Wang, Synchronous Passivation of Defects with Low Formation Energies via Terdentate Anchoring Enabling High Performance Perovskite Solar Cells with Efficiency over 24%, *Adv. Funct. Mater.*, 2022, **32**, 2200534.

56 Q. Chen, J. Wu, X. Wang, G. Li, Z. Song, Y. Xu, C. Deng, Y. D. Weihai Sun and Z. Lan, 3-Chloroperoxybenzoic acid doping spiro-OMeTAD for improving the performance of perovskite solar cells, *Chem. Eng. J.*, 2022, **450**, 138313.

57 L. Ye, P. Guo, J. Su, K. Zhang, C. Liu, P. Yang, W. Zhao, P. Zhao, Z. Liu, J. Chang, Q. Ye and H. Wang, Managing Secondary Phase Lead Iodide in Hybrid Perovskites via Surface Reconstruction for High-Performance Perovskite Solar Cells with Robust Environmental Stability, *Angew. Chem., Int. Ed.*, 2023, **62**, e202300678.

58 J. Nie, B. Niu, Y. Wang, Z. He, X. Zhang, H. Zheng, Y. Lei, P. Zhong and X. Ma, Multi-functional MXene quantum dots enhance the quality of perovskite polycrystalline films and charge transport for solar cells, *J. Colloid Interface Sci.*, 2023, **646**, 517–528.

59 Q. Sun, S. Duan, G. Liu, X. Meng, D. Hu, J. Deng, B. Shen, B. Kang and S. R. P. Silva, Porous Lead Iodide Layer Promotes Organic Amine Salt Diffusion to Achieve High Performance p–i–n Flexible Perovskite Solar Cells, *Adv. Energy Mater.*, 2023, **13**, 2301259.

60 Q. Zhou, D. He, Q. Zhuang, B. Liu, R. Li, H. Li, Z. Zhang, H. Yang, P. Zhao, Y. He, Z. Zang and J. Chen, Revealing Steric–Hindrance–Dependent Buried Interface Defect Passivation Mechanism in Efficient and Stable Perovskite Solar Cells with Mitigated Tensile Stress, *Adv. Funct. Mater.*, 2022, **32**, 2205507.

61 J. A. Kress, C. Quarti, Q. An, S. Bitton, N. Tessler, D. Beljonne and Y. Vaynzof, Persistent Ion Accumulation at Interfaces Improves the Performance of Perovskite Solar Cells, *ACS Energy Lett.*, 2022, **7**, 3302–3310.

This journal is © the Partner Organisations 2024

Inorg. Chem. Front., 2024, **11**, 3566–3577 | **3577**